Forced Wetting Transition and Bubble Pinch-Off in a Capillary Tube

Benzhong Zhao, Amir Alizadeh Pahlavan, Luis Cueto-Felgueroso, and Ruben Juanes

Phys. Rev. Lett. **120**, 084501 — Published 23 February 2018

DOI: 10.1103/PhysRevLett.120.084501

Forced wetting transition and bubble pinch-off in a capillary tube

Benzhong Zhao,[1,*] Amir Alizadeh Pahlavan,[1,†] Luis Cueto-Felgueroso,[1,2] and Ruben Juanes[1,‡]

[1]*Massachusetts Institute of Technology, 77 Massachusetts Avenue, Cambridge, Massachusetts 02139, USA*
[2]*Technical University of Madrid, Calle del Profesor Aranguren 3, 28040 Madrid, Spain*

Immiscible fluid-fluid displacement in partial wetting continues to challenge our microscopic and macroscopic descriptions. Here, we study the displacement of a viscous fluid by a less viscous fluid in a circular capillary tube in the partial wetting regime. In contrast with the classic results for complete wetting, we show that the presence of a moving contact line induces a wetting transition at a critical capillary number that is contact angle dependent. At small displacement rates, the fluid-fluid interface deforms slightly from its equilibrium state and moves downstream at a constant velocity, without changing its shape. As the displacement rate increases, however, a wetting transition occurs: the interface becomes unstable and forms a finger that advances along the axis of the tube, leaving the contact line behind, separated from the meniscus by a macroscopic film of the viscous fluid on the tube wall. We describe the dewetting of the entrained film, and show that it universally leads to bubble pinch-off, therefore demonstrating that the hydrodynamics of contact line motion generate bubbles in microfluidic devices, even in the absence of geometric constraints.

The displacement of one fluid by another immiscible fluid in small, confined geometries is an important process in many natural and industrial settings, including water infiltration into soil [1], enhanced oil recovery [2], ink-jet printing [3], and microfluidics [4]. A particularly challenging aspect of describing fluid-fluid displacement in the presence of a solid is the movement of the contact line between the two fluid phases and the solid surface (*i.e.*, the three-phase contact line), which violates the no-slip boundary condition commonly assumed in classical fluid mechanics [5–10]. Recent experiments in quasi-2D geometries [11, 12] have demonstrated that the presence of moving contact lines lead to a wealth of pattern formation regimes. Due to the planar nature of these experiments, however, the contact line could not be directly visualized.

A capillary tube provides an ideal experimental system for studying fluid-fluid displacement, as it allows for unobstructed visualization of the contact line dynamics. While the displacement of a less viscous fluid by a more viscous one has been extensively studied in the context of capillary rise [13–16] and forced imbibition [17–19], experiments on the displacement of a more viscous fluid by a less viscous one have been relatively scarce. In his seminal work, G. I. Taylor found that as the air invades into a capillary tube initially filled with a *perfectly wetting*, viscous fluid, it leaves a film of the defending fluid coating the tube walls in its wake, whose thickness is controlled by the finger velocity [20].

Here, we revisit the Taylor–Bretherton problem in the *partial wetting* regime by studying the invasion of air into a capillary tube filled by a viscous fluid, and show that contact line motion leads to novel flow behaviors. At low displacement rates, the fluid-fluid interface moves downstream at a constant velocity, without changing its shape. As the flow rate increases beyond a critical value, however, a forced wetting transition occurs and a liquid film is deposited on the tube wall. The deposited film is unstable and dewets from the wall, leading to the formation of a growing dewetting rim that ultimately causes bubble pinch-off.

We conduct fluid-fluid displacement experiments in precision-made borosilicate glass capillary tubes with inner diameter $d = 750$ μm. The capillary tube is open to the atmosphere on one end and connected to a syringe pump on the other. We fill the capillary tube with glycerol and then withdraw the glycerol so that air displaces glycerol at atmospheric pressure. Glycerol is partially wetting to the capillary tubes, and has a static receding contact angle $\theta_{\text{eq}} = 25 \pm 5^\circ$. To alter the wettability of the capillary tubes, we apply heat-assisted chemical vapor deposition (CVD) of trichlorosilane in a vacuum oven. Glycerol is less wetting to the silane-coated capillary tubes, and it has a static receding contact angle $\theta_{\text{eq}} = 68 \pm 5^\circ$. We use each capillary tube only once to ensure precise control over its wettability [21].

Figure 1 shows an experimental phase diagram of the fluid-fluid interface profiles obtained under the two distinct wettability conditions and a wide range of capillary numbers (Ca). We define $\text{Ca} = \mu U/\gamma$, where $\mu = 1400$ mPa $\cdot$ s is the viscosity of glycerol at 20°C, $U = 4Q/(\pi d^2)$ is the displacement velocity, with Q being the imposed flow rate, and $\gamma = 65 \pm 2$ mN/m is the glycerol-air interfacial tension. The left column shows the results corresponding to the more wetting case ($\theta_{\text{eq}} = 25^\circ$). At low Ca numbers, the fluid-fluid interface deforms slightly from its equilibrium state and travels downstream at a constant velocity, without changing its shape (Fig. 1a-d). Deformation of the fluid-fluid interface corresponds to a decrease in the apparent contact angle, which reaches zero at a critical capillary number Ca^*. This value of Ca^* marks the onset of the wetting transition, beyond which the defending liquid is forced to wet the tube walls as a thin film and the air advances as a finger through the center of the tube (Fig. 1e-j). We find that the onset of the wetting transition is strongly dependent on the wettability of the capillary tube: Ca^* is over an order of magnitude larger in the less wetting tube (Fig. 1, right column) compared to that in the more wetting tube (Fig. 1r vs. Fig. 1e).

The flow dynamics before the wetting transition ($\text{Ca}<\text{Ca}^*$) is governed by the two-way coupling between the fluid-fluid interface shape and the flow field within each fluid phase, as described by the Stokes equations. The Laplace pressure jump across the fluid-fluid interface is balanced by a normal viscous

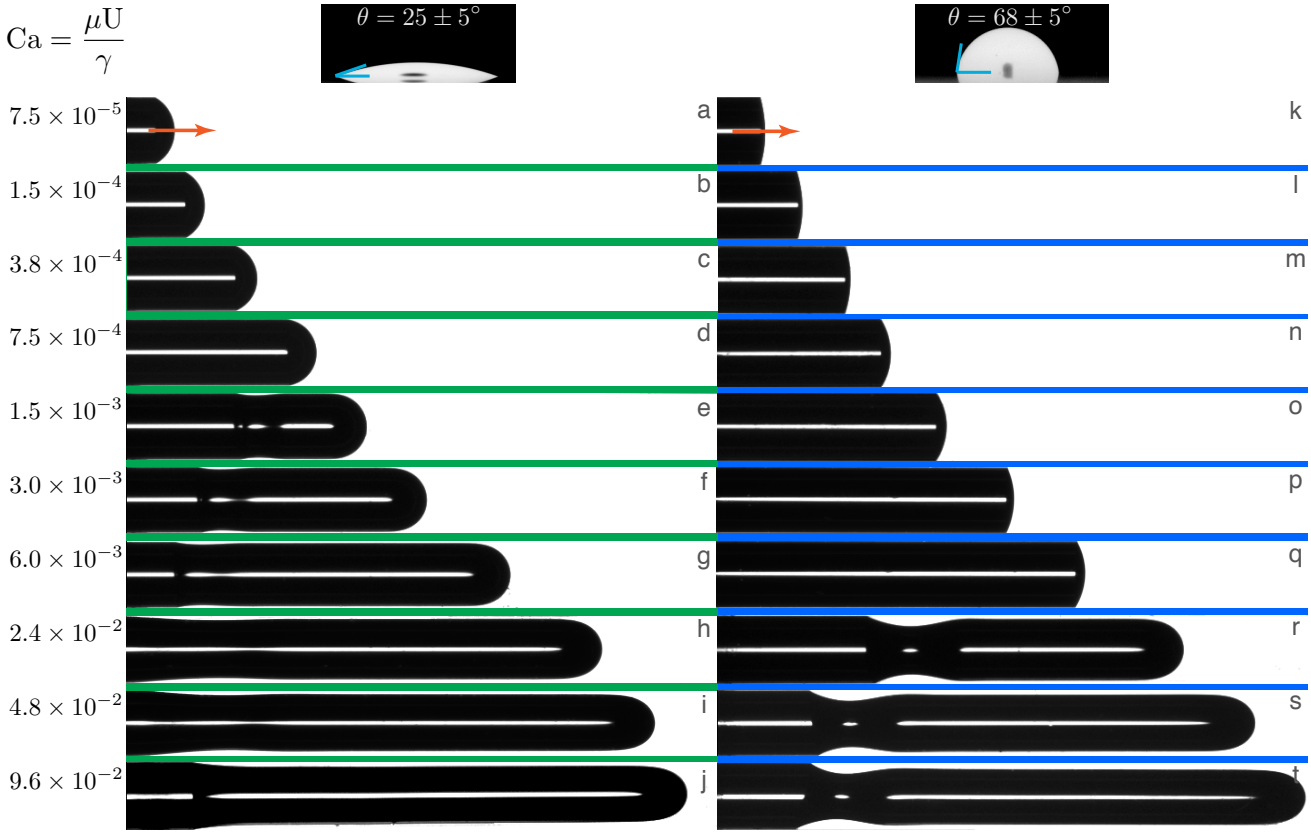

FIG. 1. Fluid-fluid interface of air (black) displacing glycerol (white) under increasing capillary numbers (top to bottom) in a wetting capillary tube with $\theta_{eq} = 25 \pm 5^\circ$ (left column) and a weakly wetting capillary tube with $\theta_{eq} = 68 \pm 5^\circ$ (right column). The orange arrows indicate the direction of interface displacement. At small Ca, the meniscus deforms slightly from its equilibrium shape, but remains as a spherical cap. At large Ca, however, a wetting transition occurs and the invading air forms a single finger that advances along the center of the tube, leaving a macroscopic trailing film of the viscous liquid on the tube walls. The critical capillary number Ca^* at which film formation occurs is controlled by the wettability (pane r vs. pane e).

stress discontinuity. In the framework of the generalized lubrication approximation [22, 23], we can use the local approximation of the Stokes flow in a wedge, for which exact analytical solutions exist [5], and greatly reduce the complexity of this problem to an equation for the shape of the interface in the frame co-moving with the fluid-fluid interface [11]. While this approximation is strictly valid for flow in a 2D setting, our results show that it provides good estimates for flow in an axisymmetric tube as well [21]. In this framework, we arrive at the following differential equation describing the interface shape:

$$\frac{d^2\theta}{ds^2} = \frac{3\mathrm{Ca} f(\theta, R)}{h(h + 3\lambda_s)}, \tag{1}$$

where θ is the local interface slope, s is the arc length along the interface, $R = \mu_g/\mu_l$ is the viscosity ratio between the gas and liquid, and $\lambda_s = \mathrm{O(nm)}$ is the slip length that removes the moving contact line singularity [5]. In the limit of zero viscosity ratio (i.e. neglecting the air viscosity), we have $f(\theta, 0) = -(2/3)(\sin\theta)^3/(\theta - \sin\theta\cos\theta)$. We can then describe the fluid-fluid interface shape deformation for an arbitrary displacement rate by solving Eq. (1) using the boundary conditions $\theta|_{s=0} = \theta_{eq}$, $h|_{s=0} = 0$ at the contact line, and $\theta|_{s=l} = \pi/2$, $h|_{s=l} = d/2$ at the tube center, where l is the half-arc length of the interface. We find excellent agreement between the experimental data and the theoretical predictions for the fluid-fluid interface shape before the wetting transition (Fig. 2). The deformation of the interface from equilibrium is accompanied by a decrease in the apparent contact angle θ_{app}. At the point of wetting transition, $\theta_{\mathrm{app}} \to 0$, and the liquid becomes effectively wetting to the walls, leaving an entrained liquid film (Fig. 2b). A similar behavior is also observed in the forced wetting transition dynamics of receding contact lines in unconfined systems when a fiber or plate is withdrawn from a liquid bath. When the liquid is perfectly wetting to the substrate, it immediately leaves a film behind, known as the Landau–Levich film [24–26]. When the liquid is only partially wetting, however, a critical plate velocity is needed for the liquid to coat the substrate [9, 27–29]. In the reverse process of forced wetting transition in advancing contact lines, air is entrained, but at much higher contact line velocities [30–37].

Below the wetting transition, the contact line moves with the same velocity as the interface tip. Above the critical point

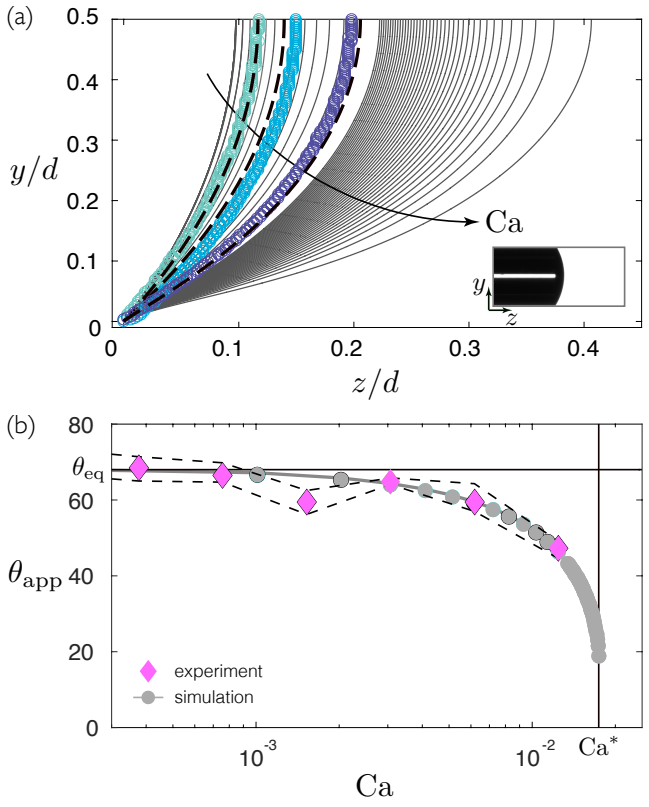

FIG. 2. (a) Fluid-fluid interface profiles for Ca<Ca* in the less wetting capillary tube ($\theta_{eq} = 68^\circ$). As Ca increases, the fluid-fluid interface deforms further from its equilibrium shape. The symbols and dashed lines correspond to the experimental and numerical results for Ca $= 0.003, 0.006, 0.012$, respectively. (b) Deformation of the fluid-fluid interface can be quantified by the apparent contact angle θ_{app}, which decreases asymptotically towards zero as the Ca approaches the critical capillary number Ca*. This marks the onset of the wetting transition. The diamond and circle symbols represent the experimental data and theoretical predictions, respectively. The dashed lines above and below the data points represent the experimental uncertainty.

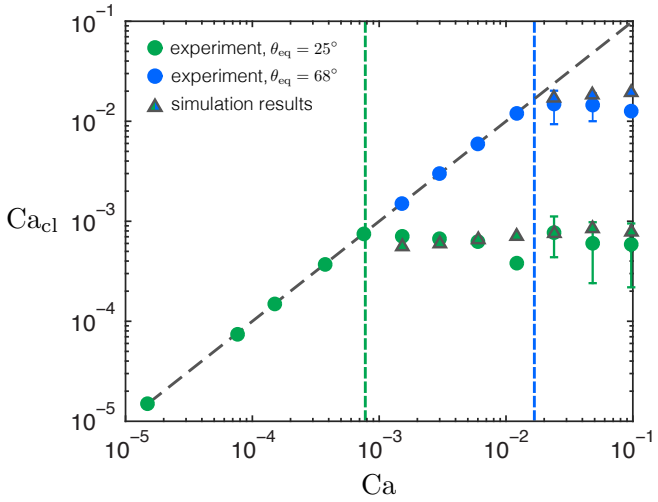

FIG. 3. The contact line capillary number $\mathrm{Ca_{cl}} = \mu U_{cl}/\gamma$ as a function of the macroscopic capillary number Ca $= \mu U/\gamma$, where U_{cl} and U are the contact line velocity and the displacement velocity, respectively. The green and blue circles represent the experimental measurements in the more wetting tube ($\theta_{eq} = 25^\circ$) and in the less wetting tube ($\theta_{eq} = 68^\circ$), respectively. The triangles show the corresponding theoretical predictions of Eq. (2). The vertical dashed lines represent the critical capillary numbers Ca* as predicted by Eq. (1). For Ca $<$ Ca*, the fluid-fluid interface deforms slightly while remaining a spherical cap, and the contact line and the interface tip travel at the imposed displacement velocity $U = 4Q/\pi d^2$ (gray dashed line). For Ca $>$ Ca*, the air forms a finger that advances along the center of the tube, leaving behind a film of the more-viscous defending liquid. The incomplete displacement of the defending liquid results in an interface tip velocity that is faster than the imposed displacement velocity. The contact line that trails behind travels at a velocity that, remarkably, is independent of the imposed flow rate. Instead, the contact line velocity is controlled by the wettability of the capillary tube.

(Ca>Ca*), however, the interface becomes unstable and a finger is formed. In this regime, the contact line travels at a constant, but smaller, velocity compared to that of the finger tip, which gives rise to a macroscopic film of the viscous defending fluid in the wake of the the finger. It is remarkable that, for Ca>Ca*, the contact line speed becomes independent of Ca (Fig. 3). This indicates that the dynamics downstream (near the finger tip) and upstream (close to the contact line) become effectively decoupled. We further observe that the contact line speed beyond the wetting transition is strongly dependent on the wettability—the contact line speed is more than an order of magnitude higher in the less wetting tube compared to that in the more wetting tube. These observations lead us to hypothesize that the dynamics of the entrained film next to the contact line can be analyzed independently of the finger tip dynamics.

The contact line behind the entrained film recedes from the tube wall at a constant rate, leading to the formation of a dewetting rim (see, *e.g.*, Fig. 1r). While the dynamics of hole formation and the associated dewetting rims has been extensively studied in the context of thin film on flat substrates [38–40], much less is known about the influence of confinement on the dewetting dynamics. In particular, as we show below, an important distinguishing factor in dewetting in confined geometries is that it leads to a pinch-off instability in finite time.

Using the long-wave approximation, we derive a model that describes the dynamics of the dewetting rim in an axisymmetric capillary tube [21]:

$$\frac{\partial \tilde{h}}{\partial \tilde{t}} = \frac{1}{(1-\tilde{h})}\frac{\partial}{\partial \tilde{z}}\left(\mathcal{M}(\tilde{h})\frac{\partial}{\partial \tilde{z}}\left[\Pi(\tilde{h}) - \tilde{\kappa}\right]\right), \qquad (2)$$

where $\tilde{h}$ is the film height measured from the tube wall, $\mathcal{M}(\tilde{h}) = 1 - 4(1-\tilde{h})^2 + 3(1-\tilde{h})^4 - 4(1-\tilde{h})^4 \ln(1-\tilde{h})$ is the mobility, $\Pi(\tilde{h}) = 6(1-\cos\theta_{eq})(\delta^2/\tilde{h}^3)(1-\delta/\tilde{h})$ is the disjoining pressure with δ as the precursor film thickness, and $\tilde{\kappa} = 1/(1-\tilde{h}) + \tilde{h}_{\tilde{z}\tilde{z}}$ is the curvature. Here, all length scales are non-dimensionalized by the tube radius r, and the dimensionless time is defined as $\tilde{t} = (\gamma/\mu)t/(8d)$. In the absence of

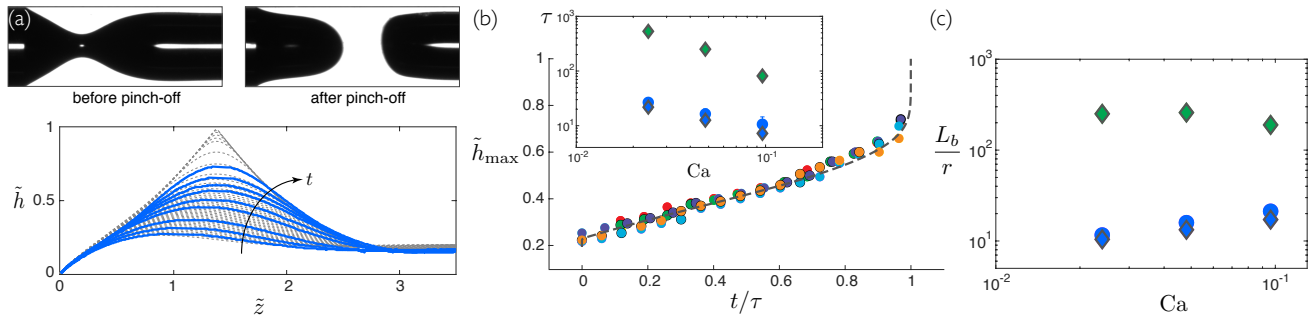

FIG. 4. (a) Top: Experimental images of the fluid-fluid interface profile just before and after pinch-off. Bottom: The dewetting rim profile in the frame co-moving with the receding contact line for Ca $= 0.096$ and $\theta_{\text{eq}} = 68^o$. The dashed and solid lines correspond to the numerical and experimental data, respectively. (b) The maximum height of the rim $\tilde{h}_{\max}$ grows linearly at early times and nonlinearly accelerates close to the pinch-off time τ. The color-coded circles represent different experimental realizations of rim growth that led to pinch-off, while the dashed line represents the theoretical prediction of Eq. (2). The inset shows the pinch-off time as a function of the capillary number and the wettability condition, where the green and blue symbols correspond to $\theta_{\text{eq}} = 25^\circ$ and 68°, respectively. The theoretical predictions (diamonds) matches closely to the experimental data (circles) for $\theta_{\text{eq}} = 68^\circ$. Given the limited experimental window, we did not directly observe pinch-off in the more wetting tube since its τ is predicted to be over an order of magnitude larger than that in the less wetting tube. (c) The bubble length L_b as a function of the capillary number and the wettability condition, where the green and blue symbols correspond to $\theta_{\text{eq}} = 25^\circ$ and 68°, respectively. The theoretical predictions (diamonds) agree well with the experimental data (circles) for $\theta_{\text{eq}} = 68^\circ$. See video [21].

the disjoining pressure, this model has similarities to the class of models describing the evolution of films coating cylindrical fibers or interior of tubes [25, 41, 42], and in the thin-film limit simplifies to the models describing the Rayleigh–Plateau instability of thin liquid films in cylindrical tubes [43, 44]. It is interesting to note that, in this limit, the model is equivalent to one describing the Rayleigh–Taylor instability of a thin film on the underside of a horizontal plate, where gravity plays the destabilizing role of the azimuthal curvature in the tube [45].

The thickness of the entrained liquid film depends on the finger tip velocity and has been determined using a matched-asymptotic analysis by Bretherton [20], who found that $h_{\text{f}} \sim \text{Ca}_{\text{f}}^{2/3}$ as Ca $\to 0$, with $\text{Ca}_{\text{f}} = \mu U_{\text{f}}/\gamma$ representing the finger capillary number. This scaling was later empirically extended to higher capillary numbers: $h_{\text{f}}/r = 1.34\text{Ca}_{\text{f}}^{2/3}/(1 + 1.34 \times 2.5\text{Ca}_{\text{f}}^{2/3})$ [46, 47]. This relationship, in combination with conservation of mass $Q = \pi(r - h_{\text{f}})^2 U_{\text{f}}$, determine both the entrained film thickness and the finger velocity. We use this thickness as the downstream boundary condition for Eq. (2).

The growth of the dewetting rim is well-captured by our theoretical predictions (Fig. 4a). At early times, the growth of the dewetting rim is linear in time due to the constant-speed retraction of the contact line (Fig. 3). At late times, however, this mechanism is overtaken by the surface tension driven Rayleigh–Plateau instability caused by the azimuthal curvature, leading to an accelerated growth and bubble pinch-off (Fig. 4b). The continual movement of the contact line repeats the process of ridge growth and pinch-off, leading to the formation of a train of mono-dispersed bubbles.

The pinch-off time depends on both the capillary number and the wettability of the capillary tube (Fig. 4b, inset). For a given wettability, higher Ca leads to faster pinch-off due to the thicker film deposited on the tube wall ($h_f \sim \text{Ca}_{\text{f}}^{2/3}$). For a given Ca, higher θ_{eq} leads to faster pinch-off due to the higher contact line velocity (Fig. 3) as the contact line velocity of the dewetting rim scales as θ_{eq}^3 [39, 40]. The large difference in contact line velocity, in turn, leads to a pinch-off time that is over an order of magnitude larger in the more wetting tube ($\theta_{\text{eq}} = 25^\circ$) compared to that in the less wetting tube ($\theta_{\text{eq}} = 68^\circ$).

The dependence of the pinch-off time on the wettability leads to a dependence of the generated bubble length L_b on the contact angle: for a given flow rate, a higher contact angle leads to faster pinch-off and therefore a smaller bubble (Fig. 4c). The impact of the flow rate on the bubble size is less straightforward. Higher Ca leads to a faster travelling finger, which increases the length of the bubble, but also to a thicker entrained film, which reduces the pinch-off time. The competition between these two effects lead to a weak dependence of the bubble length on the flow rate, leaving the wettability as the dominant factor controlling the bubble size.

Pinch-off induced bubble formation has a wide range of applications in microfluidic devices [4, 48]. Most existing microfluidic bubble generators rely on flow channels with geometric constrictions [49–52] or an external cross-flow [53–56] to initiate bubble pinch-off [57–59]. Recently, it has been shown that "superconfinement" can trigger a jet instability from a moving interface in the absence of geometric features, but through a mechanism that relies on thermal fluctuations in systems with ultralow surface tension [36]. Our experiments demonstrate that pinch-off will occur in smooth, uniform capillaries as a result of wettability-mediated contact line motion. We have shown that wettability and flow rate control the pinch-off time, and therefore can be used to tune the size of mono-dispersed bubbles.

This work was funded in part by the US Department of Energy (grants DE-FE0013999 and DE-SC0018357). LCF acknowledges funding from the Spanish Ministry of Econ-

omy and Competitiveness (grants RYC-2012-11704 and CTM2014-54312-P). LCF and RJ acknowledge funding from the MIT International Science and Technology Initiatives.

* These authors contributed equally to this work; Present address: University of Toronto, 5 King's College Road, Toronto, Ontario M5S 3G8, Canada
† These authors contributed equally to this work
‡ juanes@mit.edu

[1] L. Cueto-Felgueroso and R. Juanes, Phys. Rev. Lett. **101**, 244504 (2008).
[2] F. Orr and J. Taber, Science **224**, 563 (1984).
[3] D. Jang, D. Kim, and J. Moon, Langmuir **25**, 2629 (2009).
[4] G. M. Whitesides, Nature **442**, 368 (2006).
[5] C. Huh and L. E. Scriven, J. Colloid Interface Sci. **35**, 85 (1971).
[6] A. L. Bertozzi, Notices of the AMS **45**, 689 (1998).
[7] A. J. Briant, A. J. Wagner, and J. M. Yeomans, Phys. Rev. E **69**, 031602 (2004).
[8] A. J. Briant and J. M. Yeomans, Phys. Rev. E **69**, 031603 (2004).
[9] D. Bonn, J. Eggers, J. Indekeu, J. Meunier, and E. Rolley, Rev. Mod. Phys. **81**, 739 (2009).
[10] A. Alizadeh Pahlavan, L. Cueto-Felgueroso, G. H. McKinley, and R. Juanes, Phys. Rev. Lett. **115**, 034502 (2015).
[11] B. Levaché and D. Bartolo, Phys. Rev. Lett. **113**, 044501 (2014).
[12] B. Zhao, C. W. MacMinn, and R. Juanes, Proc. Natl. Acad. Sci. USA **113**, 10251 (2016).
[13] E. W. Washburn, Phys. Rev. **17**, 273 (1921).
[14] N. Fries and M. Dreyer, J. Colloid Interface Sci. **327**, 125 (2008).
[15] B. V. Zhmud, F. Tiberg, and K. Hallstensson, J. Colloid Interface Sci. **228**, 263 (2000).
[16] A. Siebold, M. Nardin, J. Schultz, A. Walliser, and M. Oppliger, Colloids Surf., A **161**, 81 (2000).
[17] R. L. Hoffman, J. Colloid Interface Sci. **50**, 228 (1975).
[18] R. L. Hoffman, J. Colloid Interface Sci. **94**, 470 (1983).
[19] M. Fermigier and P. Jenffer, J. Colloid Interface Sci. **146**, 226 (1991).
[20] F. P. Bretherton, J. Fluid Mech. **10**, 166 (1961).
[21] See supplemental material.
[22] J. H. Snoeijer, Phys. Fluids **18**, 021701 (2006).
[23] T. S. Chan, S. Srivastava, A. Marchand, B. Andreotti, L. Biferale, F. Toschi, and J. H. Snoeijer, Phys. Fluids **25**, 074105 (2013).
[24] B. Levich and L. Landau, Acta Physiochim. **17**, 42 (1942).
[25] D. Quéré, Annu. Rev. Fluid Mech. **31**, 347 (1999).
[26] H. A. Stone, J. Fluid Mech. **645**, 1 (2010).
[27] J. Eggers, Phys. Rev. Lett. **93**, 094502 (2004).
[28] J. H. Snoeijer, G. Delon, M. Fermigier, and B. Andreotti, Phys. Rev. Lett. **96**, 174504 (2006).
[29] J. H. Snoeijer and B. Andreotti, Annu. Rev. Fluid Mech. **45**, 269 (2013).
[30] C. Duez, C. Ybert, C. Clanet, and L. Bocquet, Nat. Phys. **3**, 180 (2007).
[31] R. Ledesma-Aguilar, R. Nistal, A. Hernández-Machado, and I. Pagonabarraga, Nat. Mater. **10**, 367 (2011).
[32] A. Marchand, T. S. Chan, J. H. Snoeijer, and B. Andreotti, Phys. Rev. Lett. **108**, 204501 (2012).
[33] E. Vandre, M. S. Carvalho, and S. Kumar, J. Fluid Mech. **707**, 496 (2012).
[34] R. Ledesma-Aguilar, A. Hernández-Machado, and I. Pagonabarraga, Phys. Rev. Lett. **110**, 264502 (2013).
[35] E. Vandre, M. S. Carvalho, and S. Kumar, J. Fluid Mech. **747**, 119 (2014).
[36] S. A. Setu, R. P. A. Dullens, A. Hernández-Machado, I. Pagonabarraga, D. G. A. L. Aarts, and R. Ledesma-Aguilar, Nat. Commun. **6**, 7297 (2015).
[37] J. E. Sprittles, Phys. Rev. Lett. **118**, 114502 (2017).
[38] C. Redon, F. Brochard-Wyart, and F. Rondelez, Phys. Rev. Lett. **66**, 715 (1991).
[39] J. H. Snoeijer and J. Eggers, Phys. Rev. E **82**, 056314 (2010).
[40] A. M. J. Edwards, R. Ledesma-Aguilar, M. I. Newton, C. V. Brown, and G. McHale, Sci. Adv. **2**, e1600183 (2016).
[41] R. V. Craster and O. K. Matar, Rev. Mod. Phys. **81**, 1131 (2009).
[42] R. Camassa and H. R. Ogrosky, J. Fluid Mech. **772**, 569 (2015).
[43] P. S. Hammond, J. Fluid Mech. **137**, 363 (1983).
[44] P. Gauglitz and C. Radke, Chem. Eng. Sci. **43**, 1457 (1988).
[45] A. Oron, S. H. Davis, and S. G. Bankoff, Rev. Mod. Phys. **69**, 931 (1997).
[46] P. Aussillous and D. Quéré, Phys. Fluids **12** (2000).
[47] E. Klaseboer, R. Gupta, and R. Manica, Phys. Fluids **26**, 032107 (2014).
[48] J. J. Agresti, E. Antipov, A. R. Abate, K. Ahn, A. C. Rowat, J.-C. Baret, M. Marquez, A. M. Klibanov, A. D. Griffiths, and D. A. Weitz, Proc. Natl. Acad. Sci. USA **107**, 4004 (2010).
[49] D. R. Link, S. L. Anna, D. A. Weitz, and H. A. Stone, Phys. Rev. Lett. **92**, 054503 (2004).
[50] P. Garstecki, I. Gitlin, W. DiLuzio, G. M. Whitesides, E. Kumacheva, and H. A. Stone, Appl. Phys. Lett. **85**, 2649 (2004).
[51] B. Dollet, W. van Hoeve, J.-P. Raven, P. Marmottant, and M. Versluis, Phys. Rev. Lett. **100**, 034504 (2008).
[52] S. Roman, M. O. Abu-Al-Saud, T. Tokunaga, J. Wan, A. R. Kovscek, and H. A. Tchelepi, J. Colloid Interface Sci. **507**, 279 (2017).
[53] T. Thorsen, R. W. Roberts, F. H. Arnold, and S. R. Quake, Phys. Rev. Lett. **86**, 4163 (2001).
[54] S. L. Anna, N. Bontoux, and H. A. Stone, Appl. Phys. Lett. **82**, 364 (2003).
[55] P. Garstecki, M. J. Fuerstman, H. A. Stone, and G. M. Whitesides, Lab Chip **6**, 437 (2006).
[56] V. van Steijn, C. R. Kleijn, and M. T. Kreutzer, Phys. Rev. Lett. **103**, 214501 (2009).
[57] C. N. Baroud, F. Gallaire, and R. Dangla, Lab Chip **10**, 2032 (2010).
[58] R. Seemann, M. Brinkmann, T. Pfohl, and S. Herminghaus, Rep. Prog. Phys. **75**, 016601 (2012).
[59] S. L. Anna, Annu. Rev. Fluid Mech. **48**, 285 (2016).